energies

MDPI

Article

Robust Predictive Power Control of *N**3-Phase PMSM for Flywheel Energy Storage Systems Application

Wenjuan Zhang [1,2], Yu Li [2,*], Gongping Wu [2], Zhimeng Rao [2], Jian Gao [2,*] and Derong Luo [2]

[1] College of Electrical and Information Engineering, Changsha University, Changsha 410082, China; z20141074@ccsu.edu.cn
[2] College of Electrical and Information Engineering, Hunan University, Changsha 410082, China; gongping_wu@hnu.edu.cn (G.W.); zhimeng_rao@hnu.edu.cn (Z.R.); hdldr@hnu.edu.cn (D.L.)
* Correspondence: liyu_cr7@hnu.edu.cn (Y.L.); Gaojian0895@hnu.edu.cn (J.G.); Tel.: +86-1869-2208-506 (J.G.)

Abstract: In this study, a robust predictive power control (R-PPC) method for an *N**3-phase permanent magnet synchronous motor (PMSM) is developed in the field of flywheel energy storage systems application, which can effectively improve robustness against inductance parameter mismatch and compensate for the one-beat delay. Firstly, the mathematical model of the *N**3-phase PMSM is illustrated, and the topological structure of the *N**3-phase PMSM is established. The R-PPC method of the *N**3-phase PMSM is then proposed by using the d–q axis current robust predictive control theory. Robustness factors are adopted to modify the current response values in the proposed robust predictive power controller, which can obtain excellent current control performance under the inductance parameter mismatch. Moreover, the next current predicted value is used to replace the current sampled value in the proposed R-PPC method to eliminate the one-beat delay. Finally, comparative simulation and experimental results verify that the proposed R-PPC method can achieve excellent current track performance and smaller torque ripple under both the charge state and discharge state.

Keywords: *N**3-phase permanent magnet synchronous motor (PMSM); robust predictive power control; inductance parameter mismatch

check for updates

Citation: Zhang, W.; Li, Y.; Wu, G.; Rao, Z.; Gao, J.; Luo, D. Robust Predictive Power Control of *N**3-Phase PMSM for Flywheel Energy Storage Systems Application. *Energies* **2021**, *14*, 3684. https://doi.org/10.3390/en14123684

Academic Editor: Armando Pires

Received: 26 April 2021
Accepted: 15 June 2021
Published: 21 June 2021

Publisher's Note: MDPI stays neutral with regard to jurisdictional claims in published maps and institutional affiliations.

Copyright: © 2021 by the authors. Licensee MDPI, Basel, Switzerland. This article is an open access article distributed under the terms and conditions of the Creative Commons Attribution (CC BY) license (https://creativecommons.org/licenses/by/4.0/).

1. Introduction

With the increasing demand for higher power energy storage motor drives, multi-phase PMSMs, commonly used as energy storage motors, are becoming widely used in flywheel energy storage systems due to their strong fault tolerance and high operating efficiency [1–4]. Despite multi-phase PMSM having many advantages, the highly efficient control of multi-phase PM motors is rather challenging because the multi-phase PMSM is a nonlinear, strong coupling integrated control object, and, in addition, subject to parameter disturbance.

Aiming to obtain the excellent control performance of multi-phase PMSMs, aside from conventional proportional integral (PI) control [5], many advanced control strategies, such as model predictive control [6] and internal model control, have been proposed. The conventional PI control can achieve excellent steady-state control performance. However, the conventional PI control method cannot maintain the control performance of multi-phase PMSMs [7]. However, the model predictive control method has great advantages because of its ability to receive both fast dynamic and static responses and to track reference values rapidly and accurately [6]. The model predictive control method strictly depends on the physical model of multi-phase PMSMs. The model predictive control method can achieve excellent static tracking control performances. However, the model parameter mismatch leads to inaccurate voltage control vectors, due to the fact that the model predictive control method absolutely depends on the precision of the multi-phase PMSM model [8–10]. Furthermore, the one-beat delay of the digital control system also seriously degrades the performance of the predictive control system [11].

In order to overcome the influence of the one-beat delay, some advanced control methods have been proposed [12–17]. In [12], a novel predictive current control strategy was presented in order to overcome the influence of the one step delay by using the current prediction value of the next time. In [13], an improved deadbeat predictive current control method was proposed to overcome one-step control delay and parameter mismatch. In [14], a novel deadbeat predictive current control algorithm was presented, which can eliminate the influence of calculating time steps of the predictive control algorithm. In [15], a novel predictive stator flux control technique was presented to overcome parameter mismatch and the one-step delay. In [16], a robust nonlinear predictive current control strategy was presented to guarantee the performance of the predictive control system. In [17], a new predictive control algorithm with a Luenberger observer was presented, which can offer robustness against computational delay.

Model parameter mismatch is an important factor influencing the performance of the predictive control system. Model parameter mismatch occurs as a results of errors in parameter identification or high temperatures of operation. The model parameter mismatch leads to the inconsistency between the parameters in the actual motor system and those in the predictive control system, rendering predicted voltage vectors inaccurate [18]. In order to enhance robustness against model parameter mismatch, some improved predictive control methods have been presented [19–25]. In [19,20], a continuous time model predictive control method was developed by adopting the disturbance observer-based compensation technique, which can effectively deal with model parameter uncertainties in practical engineering. In [21], a novel flux immunity robust predictive current control, based on an incremental model and extended state observer, was presented, and improved inductance robustness to eliminate any predicted errors caused by stator inductance mismatch. In [22], a robust model predictive control was proposed to overcome the influence of unknown external disturbances and model uncertainties by minimizing instantaneous d- and q-axes current errors in every sampling period. In [23], a hierarchical model predictive control strategy was proposed and analyzed, which can reduce the influence of the difference between the nominal predicted dynamics system and the actual one. In [24], a novel predictive functional control method with an extended state observer was proposed to overcome external disturbance. In [25], a novel robust predictive control strategy was developed, which can achieve excellent dynamic response and strong robustness under parameter perturbation.

In this paper, a novel R-PPC method without disturbance observer for an *N**3-phase PMSM is presented in the field of flywheel energy storage systems application, which can effectively enhance robustness against inductance parameter mismatch and compensate for the influence of the one-beat delay. The *N**3-phase PMSM can achieve excellent current track performance and smaller torque ripple through the use of robustness factors. Compared with the conventional PPC method, simulation and experimental results verify that the proposed R-PPC strategy can achieve the merits of less torque ripple and lower d- and q-axis response current ripple under the inductance parameter mismatch.

This paper is organized as follows. The mathematical model of the novel *N**3-phase PMSM is established in Section 2. The topological structure of the *N**3-phase PMSM drive system is illustrated in Section 3. The robust predictive power control of novel the *N**3-phase PMSM is proposed in Section 4. The simulation results are given in Section 5, respectively. Section 6 concludes this paper.

2. The Mathematical Model of the *N**3-Phase PMSM

In this paper, an *N**3-phase PMSM is proposed to meet the capacity demand of a high power flywheel energy storage system. The *N**3-phase PMSM is composed of *N* motor units. The characteristics of these motor units are repetitious, and each motor unit has magnetic and electrical isolation characteristics. As an example, the structural diagram of a 6*3-phase PMSM is shown in Figure 1.

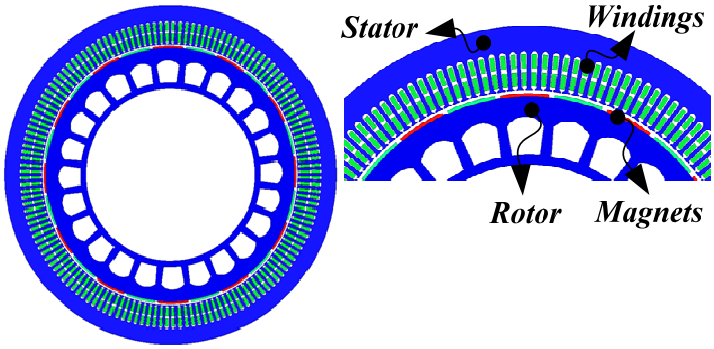

Figure 1. The structural diagram of a 6*3-phase PMSM.

The voltage equations of the *N**3-phase PMSM can be described as [2,4]:

$$\begin{cases} \frac{di_{dj}}{dt} = -\frac{R_o}{L_o} i_{dj} + \omega_e i_{qj} + \frac{1}{L_o} u_{dj} \\ \frac{di_{qj}}{dt} = -\frac{R_o}{L_o} i_{qj} - \omega_e i_{dj} - \frac{\psi_{ro}}{L_o} \omega_e + \frac{1}{L_o} u_{qj} \end{cases} \quad (1)$$

where j stands for any unit of the motor, i_{dj} and i_{qj} are the d- and q-axis currents, respectively; R_o and L_o are the stator resistance and stator inductance, respectively; ω_e is the electrical rotor speed, ψ_{ro} is the flux linkage of permanent magnets; t is the time variable; and u_{dj} and u_{qj} represent the d- and q-axis voltages of the j th winding, respectively.

The electromagnetic torque produced by the *N**3-phase PMSM can be expressed as follows:

$$T_e = \frac{3n_p}{2} \sum_{j=1}^{N} (\psi_{ro} i_{qj}) \quad (2)$$

The mechanical dynamic model of the *N**3-phase PMSM can be described as follows:

$$T_e - T_L = \frac{J}{p} \frac{d\omega_e}{dt} \quad (3)$$

where n_p is the number of pole pairs, J is the moment of inertia; and T_e and T_L are the electromagnetic torque and load torque of the *N**3-phase PMSM, respectively.

3. Topological Structure of the *N**3-Phase PMSM Drive System

In order to expand the application of the *N**3-phase PMSM in rail transit, a multi-module parallel power electronics converter energy storage system is developed in this paper. Figure 2 illustrates the topological structure of the *N**3-phase PMSM drive system.

During the braking state and starting state of the train, the *N**3-phase PMSM is respectively used as a motor and generator. In the generator mode, the flywheel storage provides energy for train acceleration through the discharge storage, while in the motor mode, it consumes the energy of the train braking through the charging storage. When the train decelerates to enter a station, the *N**3-phase PMSM is used as the motor for charging (i.e., power $P > 0$). When the train accelerates to leave the station, the *N**3-phase PMSM is used as the generator for discharging (i.e., power $P < 0$). According to the above analysis, the discharging and charging control of the *N**3-phase PMSM is essentially the power control, which can obtain excellent static control performance.

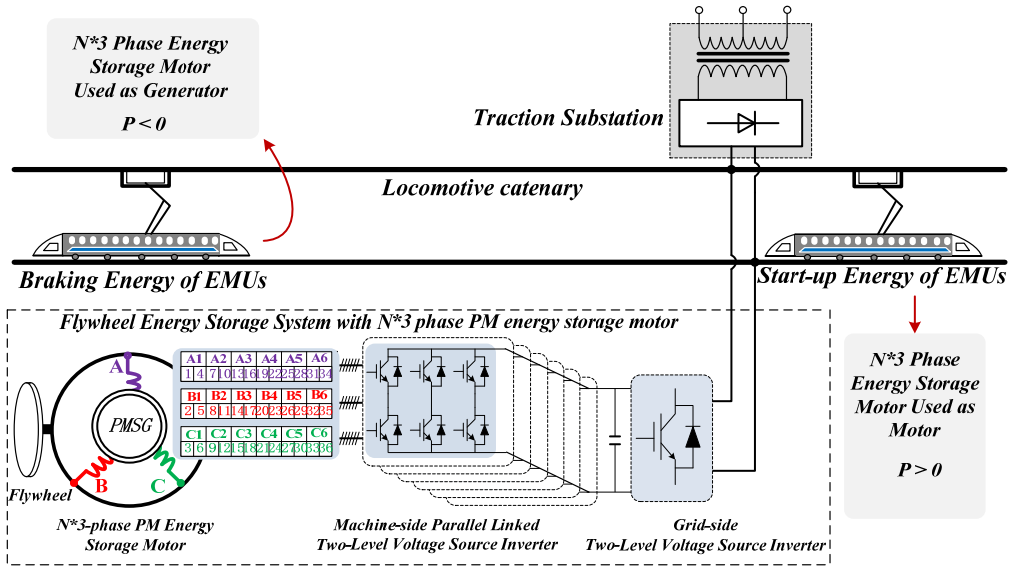

Figure 2. Topological structure of the *N**3-phase PMSM system for ground rail transit.

4. Robust Predictive Power Control of the Novel *N**3-Phase PMSM

*4.1. Drive System of the Novel N*3-Phase PMSM*

A 6*3-phase PMSM, connected with six voltage source inverters (VSIs), is used as an example as shown in Figure 3. The proposed R-PPC method of the *N**3-phase PMSM drive system is illustrated in Figure 4. According to the characteristic analyses of the 6*3-phase PMSM, it is known that the control of the VSIs can be analogous to that of a conventional VSI. In this paper, a novel R-PPC method of the *N**3-phase PMSM drive system is realized by using the d–q axis current robust predictive control. Using the robustness factors, the robust predictive current controller is adopted to modify the current response values, and the perfect current response under the inductance parameter mismatch can be obtained. In addition, the proposed R-PPC method can compensate for the one-beat delay of the digital control system by using the Smith predictor.

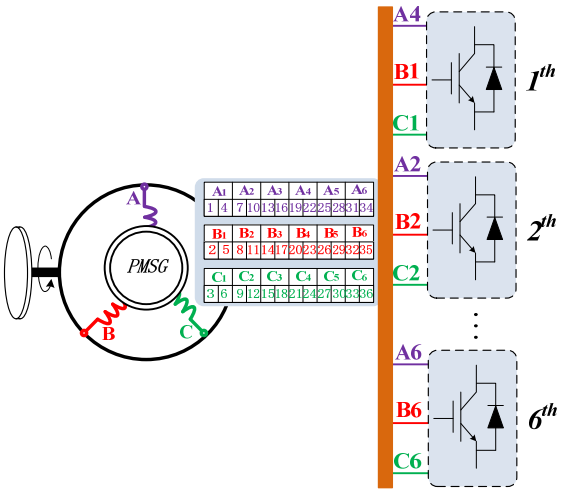

Figure 3. Connection diagram of the voltage source inverters of the 6*3-phase PMSM.

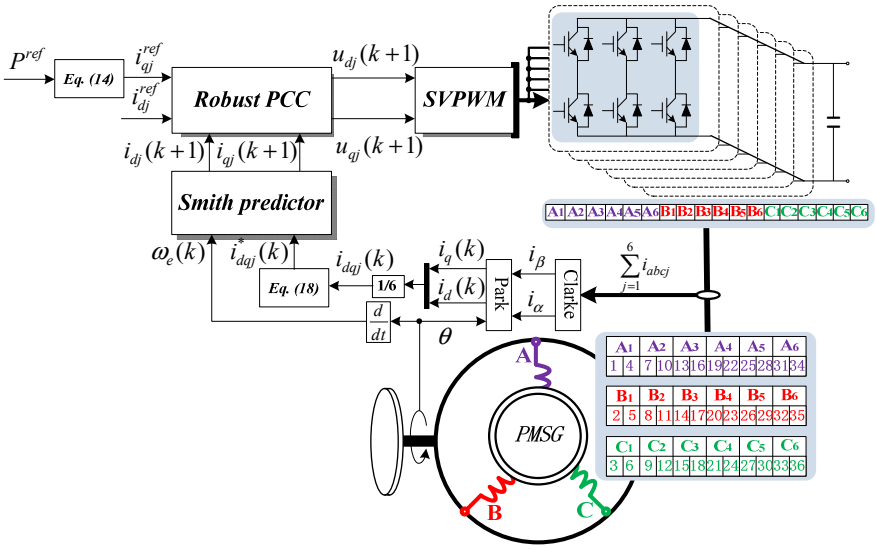

Figure 4. Robust predictive power control method of the *N**3-phase PMSM drive system.

*4.2. Discrete Form Expression of the N*3-Phase PMSM*

According to Equation (1), the general state equation of the *N**3-phase PMSM can be described as follow [18]:

$$\boldsymbol{x}_j(t) = e^{\boldsymbol{A}(t-t_o)}\boldsymbol{x}_j(t_o) + \int_{t_o}^{t} e^{\boldsymbol{A}(t-\tau)}(\boldsymbol{B}\boldsymbol{u}_j(\tau) + \boldsymbol{D})d\tau \tag{4}$$

where T_s is the sampling period, $\boldsymbol{x}_j(t) = \begin{bmatrix} i_{dj} \\ i_{qj} \end{bmatrix}$, $\boldsymbol{u}_j(t) = \begin{bmatrix} u_{dj} \\ u_{qj} \end{bmatrix}$, $\boldsymbol{A}(t) = \begin{bmatrix} -\frac{R_o}{L_o} & \omega_e \\ -\omega_e & -\frac{R_o}{L_o} \end{bmatrix}$, $\boldsymbol{B} = \begin{bmatrix} \frac{1}{L_o} & 0 \\ 0 & \frac{1}{L_o} \end{bmatrix}$, $\boldsymbol{D} = \begin{bmatrix} 0 \\ -\frac{\omega_e}{L_o}\psi_{ro} \end{bmatrix}$.

When the sampling period T_s is set as very short, we get,

$$\begin{cases} e^{-\frac{R_o T_s}{L_{do}}} \approx 1 - \frac{R_o T_s}{L_{do}} \\ e^{-\frac{R_o T_s}{L_{qo}}} \approx 1 - \frac{R_o T_s}{L_{qo}} \\ \cos(\omega_e T_s) \approx 1 \\ \sin(\omega_e T_s) \approx \omega_e T_s \end{cases} \tag{5}$$

The discrete d- and q-axis voltage equation of the *N**3-phase PMSM can be expressed as follows:

$$\begin{cases} u_{dj}(k) = \frac{L_o}{T_s} i_{dj}(k+1) + (R_o - \frac{L_o}{T_s}) i_{dj}(k) - L_o \omega_e(k) i_{qj}(k) \\ u_{qj}(k) = \frac{L_o}{T_s} i_{qj}(k+1) + (R_o - \frac{L_o}{T_s}) i_{qj}(k) + L_o \omega_e(k) i_{dj}(k) + \psi_{ro}\omega_e(k) \end{cases} \tag{6}$$

where $u_{dj}(k+1)$ and $u_{qj}(k+1)$ are the d- and q-axis of the predictive current controller output voltage, respectively; and $i_{dj}(k)$ and $i_{qj}(k)$ are the d- and q-axis current values, respectively.

According to Equation (6), the conventional current predictive controller of the *N**3-phase PMSM can be designed as follow:

$$\begin{cases} u_{dj}(k) = \frac{L_o}{T_s} i_{dj}^{ref} + (R_o - \frac{L_o}{T_s}) i_{dj}(k) - L_o \omega_e(k) i_{qj}(k) \\ u_{qj}(k) = \frac{L_o}{T_s} i_{qj}^{ref} + (R_o - \frac{L_o}{T_s}) i_{qj}(k) + L_o \omega_e(k) i_{dj}(k) + \psi_{ro}\omega_e(k) \end{cases} \tag{7}$$

where i_{dj}^{ref} and i_{qj}^{ref} are the d- and q-axis current reference values, respectively.

4.3. Sensitivity Analysis of Inductance Parameter Mismatch

Under normal conditions, the voltage equation of the N*3-phase PMSM can be described as:

$$\begin{cases} u_{dj} = R_o i_{dj} + \frac{d\psi_{dj}}{dt} - \omega_e \psi_{qj} \\ u_{qj} = R_o i_{qj} + \frac{d\psi_{qj}}{dt} + \omega_e \psi_{dj} \end{cases} \tag{8}$$

Under normal conditions, the d- and q-axis flux linkage is:

$$\begin{cases} \psi_{dj} = \psi_{ro} + L_o i_{dj} \\ \psi_{qj} = L_o i_{qj} \end{cases} \tag{9}$$

The d- and q-axis flux linkage under the inductance parameter mismatch can be expressed as:

$$\begin{cases} \psi_d = \psi_{ro} + (L_o + \Delta L) i_d \\ \psi_q = (L_o + \Delta L) i_q \end{cases} \tag{10}$$

By substituting Equation (10) into Equation (1), the state equation of the N*3-phase PMSM under the inductance parameter mismatch can be obtained as:

$$\frac{d\boldsymbol{x}}{dt} = \boldsymbol{A}\boldsymbol{x} + \boldsymbol{B}\boldsymbol{u} + \boldsymbol{D}\boldsymbol{f_a} - \boldsymbol{B}\boldsymbol{f} \tag{11}$$

where $\boldsymbol{x} = \begin{bmatrix} i_d \\ i_q \end{bmatrix}$, $\boldsymbol{u} = \begin{bmatrix} u_d \\ u_q \end{bmatrix}$, $\boldsymbol{y} = \begin{bmatrix} i_d \\ i_q \end{bmatrix}$, $\boldsymbol{f_a} = \begin{bmatrix} \psi_{ro} \\ 0 \end{bmatrix}$, $\boldsymbol{f} = \begin{bmatrix} f_d \\ f_q \end{bmatrix}$, $\boldsymbol{A} = \begin{bmatrix} -\frac{R_o}{L_o} & \omega_e \frac{L_o}{L_o} \\ -\omega_e \frac{L_o}{L_o} & -\frac{R_o}{L_o} \end{bmatrix}$, $\boldsymbol{B} = \begin{bmatrix} \frac{1}{L_o} & 0 \\ 0 & \frac{1}{L_o} \end{bmatrix}$, $\boldsymbol{D} = \begin{bmatrix} 0 & \frac{\omega_e}{L_o} \\ -\frac{\omega_e}{L_o} & 0 \end{bmatrix}$.

With

$$\begin{cases} f_d = \frac{\Delta L}{(L_o + \Delta L)}(u_{dj} - R_o i_{dj} + L_o \omega_e i_{qj} + \Delta L \omega_e i_{qj}) - \Delta L \omega_e i_{qj} \\ f_q = \frac{\Delta L}{(L_o + \Delta L)}(u_{qj} - R_o i_{qj} - L_o \omega_e i_{dj} - \Delta L \omega_e i_{dj} - \omega_e \psi_{ro}) + \Delta L \omega_e i_{dj} \end{cases} \tag{12}$$

By discretizing Equation (11), the discrete state equation of N*3-phase PMSM under the inductance parameter mismatch can be obtained as:

$$\boldsymbol{i}(k+1) = \boldsymbol{E}_o(k) \cdot \boldsymbol{i}(k) + \boldsymbol{F}_o \cdot \boldsymbol{u}(k) + \boldsymbol{P}_o(k) - \boldsymbol{F}_o \boldsymbol{f}(k) \tag{13}$$

where $\boldsymbol{i}(k+1) = \begin{bmatrix} i_d(k+1) \\ i_q(k+1) \end{bmatrix}$, $\boldsymbol{i}(k) = \begin{bmatrix} i_d(k) \\ i_q(k) \end{bmatrix}$, $\boldsymbol{E}_o(k) = \begin{bmatrix} 1 - \frac{R_o}{L_o} T_s & T_s \omega_e(k) \\ -T_s \omega_e(k) & 1 - \frac{R_o}{L_o} T_s \end{bmatrix}$, $\boldsymbol{u}(k) = \begin{bmatrix} u_d(k) \\ u_q(k) \end{bmatrix}$, $\boldsymbol{F}_o = \begin{bmatrix} \frac{1}{L_o} T_s & 0 \\ 0 & \frac{1}{L_o} T_s \end{bmatrix}$, $\boldsymbol{P}_o(k) = \begin{bmatrix} 0 \\ -\frac{\psi_{ro}}{L_o} T_s \omega_e(k) \end{bmatrix}$.

With

$$\boldsymbol{f}(k) = \begin{bmatrix} f_d(k) \\ f_q(k) \end{bmatrix} = \begin{bmatrix} \frac{\Delta L}{(L_o + \Delta L)}(u_{dj}(k) - R_o i_{dj}(k) + L_o \omega_e(k) i_{qj}(k) + \Delta L \omega_e(k) i_{qj}(k)) - \Delta L \omega_e(k) i_{qj}(k) \\ \frac{\Delta L}{(L_o + \Delta L)}(u_{qj}(k) - R_o i_{qj}(k) - L_o \omega_e(k) i_{dj}(k) - \Delta L \omega_e(k) i_{dj}(k) - \omega_e(k) \psi_{ro}) + \Delta L \omega_e(k) i_{dj}(k) \end{bmatrix}$$

By substituting Equation (7) into Equation (13), the relationship between the current command value and response value under the inductance parameter mismatch can be expressed as:

$$\Delta \boldsymbol{i}(k+1) = \boldsymbol{i}(k+1) - \boldsymbol{i}^{ref}(k+1) = -\boldsymbol{F}_o \boldsymbol{f}(k) \tag{14}$$

where $-\boldsymbol{F}_o \boldsymbol{f}(k) = \begin{bmatrix} \Delta i_{dj} \\ \Delta i_{qj} \end{bmatrix} = -\begin{bmatrix} \frac{T_s}{L_o} f_d(k) \\ \frac{T_s}{L_o} f_q(k) \end{bmatrix}$.

When the *N**3-phase PMSM is running steadily, the voltage equation of the motor system can be obtained according to Equation (1):

$$\begin{cases} u_{dj}(k) = R_o i_{dj}(k) - L_o \omega_e i_{qj}(k) \\ u_{qj}(k) = R_o i_{qj}(k) + L_o \omega_e i_{dj}(k) + \omega_e \psi_{ro} \end{cases} \tag{15}$$

Combining Equations (12), (14) and (15), the current deviation of d- and q-axis flux linkage can be simplified as:

$$\begin{cases} \Delta i_{dj} = \frac{\Delta L}{(L_o + \Delta L)} T_s \omega_e i_{qj}(k) \\ \Delta i_q = 0 \end{cases} \tag{16}$$

From Equation (16), it can be known that the mismatch of inductance parameters will affect the control performance of the d-axis current, but the tracking deviation of the q-axis current is zero. However, the mismatch of inductance parameters will increase the d- and q-axis response current ripple, which will lead to torque ripple of the *N**3-phase PMSM.

4.4. Robust Predictive Power Control with One-Step Delay Compensation

From Equation (16), it can be known that the conventional current predictive controller relies heavily on the motor parameters. Especially when the inductance parameters are mismatched, the control performance of the *N**3-phase PMSM will be seriously deteriorated. In addition, there exists the one-beat delay between the reference voltage value and the actual output voltage value in the digital control system. This also degrades the performance of the predictive current controller if the one-beat delay is not eliminated in the proposed robust predictive controller. Firstly, the current response value (i.e., $i_{dj}(k+1)$, $i_{qj}(k+1)$) of the $(k+1)T_s$ moment should be obtained at the kT_s moment. The ideal voltage vector (i.e., $u_{dj}(k+1)$, $u_{qj}(k+1)$) of the kT_s moment is then calculated by using the predicted current response value (i.e., $i_{dj}(k+1)$, $i_{qj}(k+1)$). Figure 5 illustrates the principle of one-beat delay compensation of predictive controller.

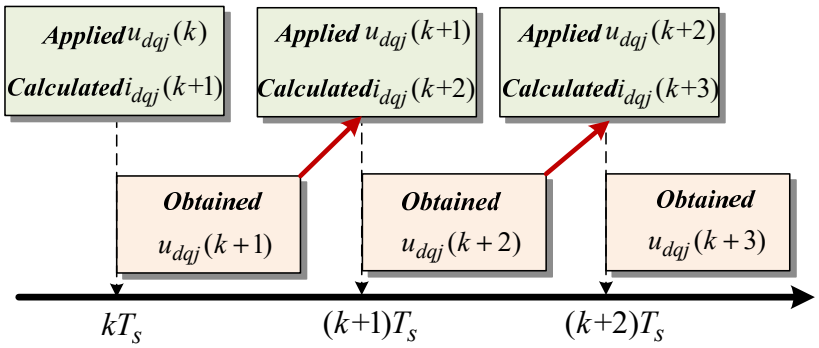

Figure 5. Principle diagram of one-beat delay compensation.

In order to eliminate the influence of one-beat delay, Equation (7) is modified to:

$$\begin{cases} u_{dj}(k+1) = \frac{L_o}{T_s} i_{dj}^{ref} + (R_o - \frac{L_o}{T_s}) i_{dj}(k+1) - L_o \omega_e(k+1) i_{qj}(k+1) \\ u_{qj}(k+1) = \frac{L_o}{T_s} i_{qj}^{ref} + (R_o - \frac{L_o}{T_s}) i_{qj}(k+1) + L_o \omega_e(k+1) i_{dj}(k+1) + \psi_{ro} \omega_e(k+1) \end{cases} \tag{17}$$

At the kT_s moment, the current response value (i.e., $i_{dj}(k+1)$, $i_{qj}(k+1)$) of the $(k+1)T_s$ moment can be calculated according to Equation (17).

$$\begin{cases} i_{qj}(k+1) = \frac{1}{L_o} T_s u_{qj}(k) - (\frac{R_o}{L_o} T_s - 1) i_{qj}(k) - T_s \omega_e(k) i_{dj}(k) - \frac{1}{L_o} T_s \psi_{ro} \omega_e(k) \\ i_{dj}(k+1) = \frac{1}{L_o} T_s u_{dj}(k) - (\frac{R_o}{L_o} T_s - 1) i_{dj}(k) - T_s \omega_e(k) i_{qj}(k) \end{cases} \tag{18}$$

From Equation (18), it can be known that the $i_{dj}(k)$, $i_{qj}(k)$, $u_{dj}(k)$, and $u_{qj}(k)$ are known quantities at the kT_s moment. Therefore, the current response value (i.e., $i_{dj}(k+1)$, $i_{qj}(k+1)$) of the $(k+1)T_s$ moment can be calculated by Equation (18). The electrical speed can be considered as constant as the electrical time is far less than the mechanical time (i.e., $\omega_e(k) = \omega_e(k+1)$). The ideal voltage vector (i.e., $u_{dj}(k+1)$, $u_{qj}(k+1)$) of the kT_s moment can be calculated by substituting Equation (18) into Equation (17).

$$\begin{bmatrix} u_{dj}(k+1) \\ u_{qj}(k+1) \end{bmatrix} = \frac{L_o}{T_s}\begin{bmatrix} i_{dj}^{ref} \\ i_{qj}^{ref} \end{bmatrix} + \frac{L_o}{T_s}\begin{bmatrix} -(1-\frac{R_o}{L_o}T_s) & -T_s\omega_e(k) \\ T_s\omega_e(k) & -(1-\frac{R_o}{L_o}T_s) \end{bmatrix}\left\{\frac{T_s}{L_o}\begin{bmatrix} u_{dj}(k) \\ u_{qj}(k) \end{bmatrix} + \begin{bmatrix} (1-\frac{R_o}{L_o}T_s) & -T_s\omega_e(k) \\ -T_s\omega_e(k) & (1-\frac{R_o}{L_o}T_s) \end{bmatrix}\begin{bmatrix} i_{dj}(k) \\ i_{qj}(k) \end{bmatrix} - \begin{bmatrix} \frac{T_s}{L_o}\psi_{ro}\omega_e(k) \\ 0 \end{bmatrix}\right\} + \begin{bmatrix} 0 \\ \psi_{ro}\omega_e(k) \end{bmatrix} \quad (19)$$

Since $1 - \frac{R_o}{L_o}T_s \approx 1$, Equation (19) is then modified to:

$$\begin{bmatrix} u_{dj}(k+1) \\ u_{qj}(k+1) \end{bmatrix} = \frac{L_o}{T_s}\begin{bmatrix} i_{dj}^{ref} \\ i_{qj}^{ref} \end{bmatrix} + \begin{bmatrix} -\frac{L_o}{T_s} & -L_o\omega_e(k) \\ L_o\omega_e(k) & -\frac{L_o}{T_s} \end{bmatrix}\left\{\frac{T_s}{L_o}\begin{bmatrix} u_{dj}(k) \\ u_{qj}(k) \end{bmatrix} + \begin{bmatrix} 1 & -T_s\omega_e(k) \\ -T_s\omega_e(k) & 1 \end{bmatrix}\begin{bmatrix} i_{dj}(k) \\ i_{qj}(k) \end{bmatrix} - \begin{bmatrix} \frac{T_s}{L_o}\psi_{ro}\omega_e(k) \\ 0 \end{bmatrix}\right\} + \begin{bmatrix} 0 \\ \psi_{ro}\omega_e(k) \end{bmatrix} \quad (20)$$

Due to the response current ripples caused by the inductance parameter mismatch, the proposed R-PPC method using the robustness factors is developed to improve the system stability and avoid the response current ripple. After using the robustness factors, the current response values of the kT_s moment can be expressed as follows:

$$\begin{cases} i_{dj}^{*}(k) = \alpha i_{dj}^{ref} + \beta i_{dj}(k) \\ i_{qj}^{*}(k) = \alpha i_{qj}^{ref} + \beta i_{qj}(k) \end{cases} \quad (21)$$

where α and β are the robustness factors, and $\alpha + \beta = 1$.

According to Equations (20) and (21), the ideal voltage vector (i.e., $u_{dj}(k+1)$, $u_{qj}(k+1)$) of the kT_s moment can be expressed as follows:

$$\begin{bmatrix} u_{dj}(k+1) \\ u_{qj}(k+1) \end{bmatrix} = \frac{L_o}{T_s}\begin{bmatrix} i_{dj}^{ref} \\ i_{qj}^{ref} \end{bmatrix} + \begin{bmatrix} -\frac{L_o}{T_s} & -L_o\omega_e(k) \\ L_o\omega_e(k) & -\frac{L_o}{T_s} \end{bmatrix}\left\{\frac{T_s}{L_o}\begin{bmatrix} u_{dj}(k) \\ u_{qj}(k) \end{bmatrix} + \begin{bmatrix} 1 & -T_s\omega_e(k) \\ -T_s\omega_e(k) & 1 \end{bmatrix}\begin{bmatrix} \alpha i_{dj}^{ref} + \beta i_{dj}(k) \\ \alpha i_{qj}^{ref} + \beta i_{qj}(k) \end{bmatrix} - \begin{bmatrix} \frac{T_s}{L_o}\psi_{ro}\omega_e(k) \\ 0 \end{bmatrix}\right\} + \begin{bmatrix} 0 \\ \psi_{ro}\omega_e(k) \end{bmatrix} \quad (22)$$

According to Equation (2), the electromagnetic torque discrete equation of the N*3-phase PMSM can be obtained as follows:

$$T_e(k) = \frac{3Nn_p}{2}\psi_{ro}i_{qj}(k) \quad (23)$$

The power discrete expression of the N*3-phase PMSM is:

$$P(k) = T_e(k)\omega_e(k) \quad (24)$$

According to Equations (23) and (24), one yields,

$$i_{qj}^{ref}(k) = \frac{2P^{ref}(k)}{3Nn_p\psi_{ro}\omega_e(k)} \quad (25)$$

where $P^{ref}(k)$ is the power reference value.

5. Simulations

The drive system structure of the 6*3-phase PMSM is designed by adopting the MATLAB/Simulink. Table 1 shows the main parameters of the 6*3-phase PMSM. The robustness factors of the proposed R-PPC method are set as $\alpha = 0.4$ and $\beta = 0.6$, respectively. During the discharging state and charging state, some simulation results of the 6*3-phase PMSM are illustrated to verify the control performance of the proposed R-PPC strategy.

Table 1. 6*3-phase PMSM.

Parameters	Value
Rated power	630 kW
Rated speed	3000 r/min
Rated speed	800 N·m
Rotational inertia (J)	100 kg·m^2
Stator phase resistance (R_o)	0.026 Ω
Number of pole pairs (n_p)	4
Inductances (L_o)	5.572 mH
Flux linkage of PM (Ψ_{ro})	0.992 Wb
Type of magnet	NdFeB
Magnet coercivity	889 kA/m
Operating temperature	20 °C

5.1. A. Control Performance Comparison between the Conventional PPC and Proposed R-PPC under the Charge State

In order to verify the R-PPC performance of the 6*3-phase PMSM in the case of charge state, the power reference of charge state is given as:

$$\begin{cases} P^{ref} = 1.6 \times 10^5 t + 0.8 \times 10^5 & 0 \le t \le 0.5s \\ P^{ref} = 1.6 \times 10^5 & 0.5s \le t \le 1s \end{cases} \quad (26)$$

In this simulation, the inductance parameter values are stepped to 50% of their initial values to simulate the inductance parameter mismatch. Comparison simulation results of the conventional PPC and proposed R-PPC under the inductance parameter mismatch are given in Figures 6–10. Figure 6 shows the comparative simulation results of the phase current and torque by using the conventional PPC and the proposed R-PPC. It can be seen from Figure 6a that the peak-to-peak torque ripple of the 6*3-phase PMSM reaches ±250 N·m in comparison to the conventional PPC method. From Figure 6b, it can be seen that the peak-to-peak torque ripple of the proposed R-PPC is reduced to ±140 N·m, which is obviously lower than that of the conventional PPC method. From Figure 6, it is known that the inductance parameter mismatch has a great influence on the torque control performance in the conventional PPC method.

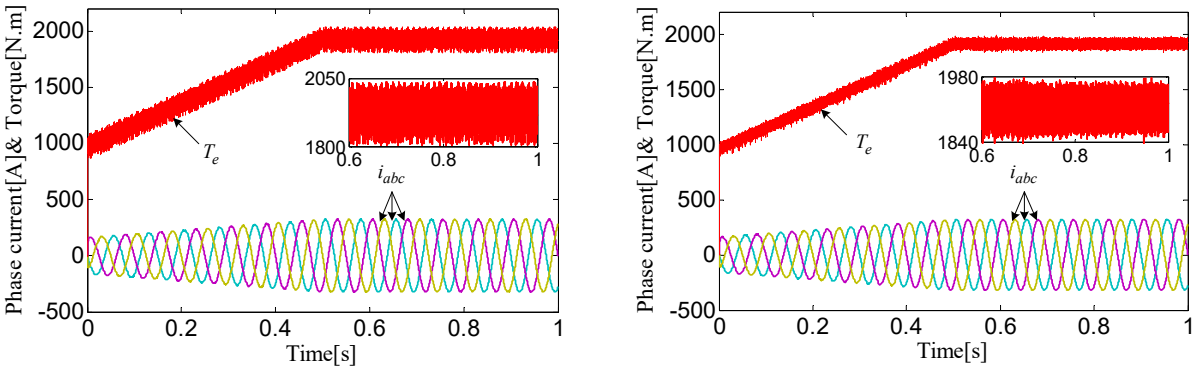

(**a**) Conventional PPC method (**b**) Proposed R-PPC method

Figure 6. Simulation results of the phase current and torque under the charge state. (**a**) Conventional PPC method; (**b**) Proposed R-PPC method.

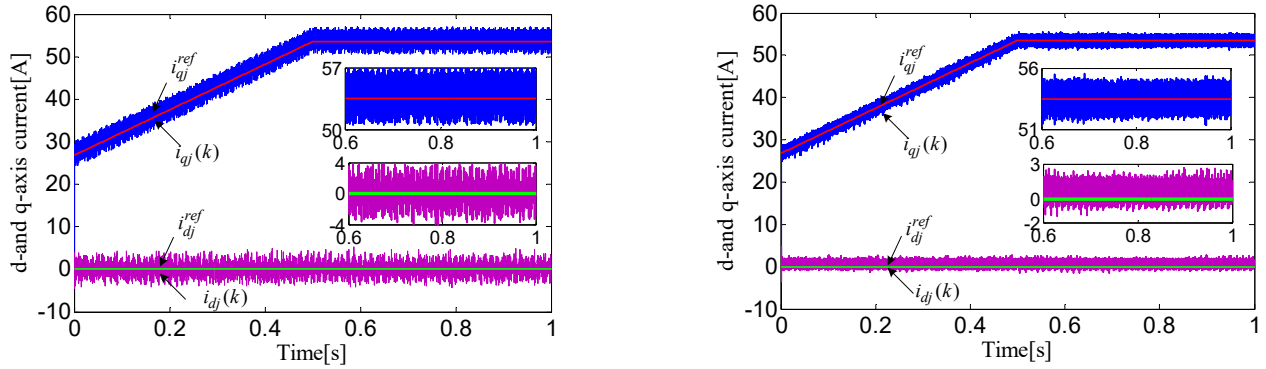

(**a**) Conventional PPC method (**b**) Proposed R-PPC method

Figure 7. Simulation results of the d- and q-axis current under the charge state. (**a**) Conventional PPC method; (**b**) Proposed R-PPC method.

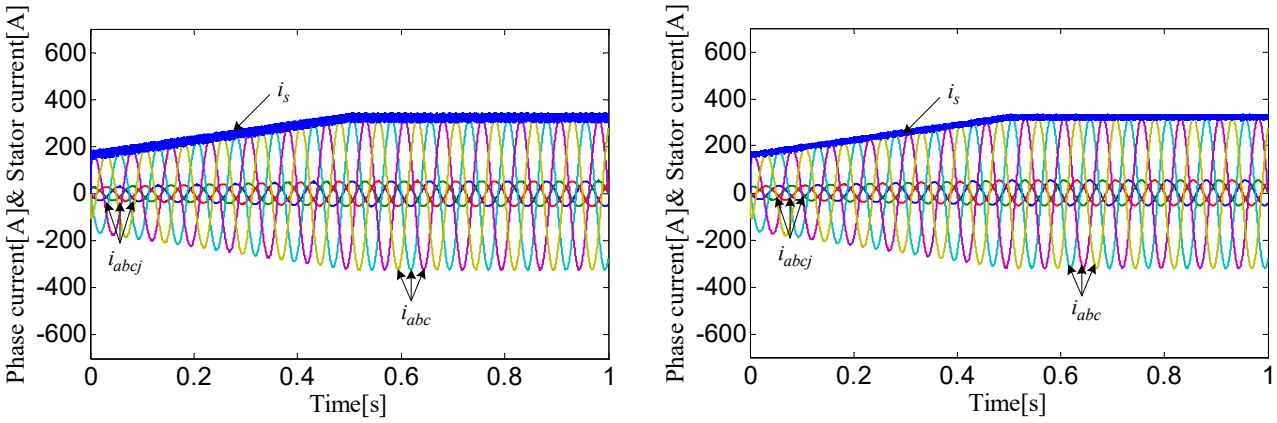

(**a**) Conventional PPC method (**b**) Proposed R-PPC method

Figure 8. Simulation results of the phase current under the charge state. (**a**) Conventional PPC method; (**b**) Proposed R-PPC method.

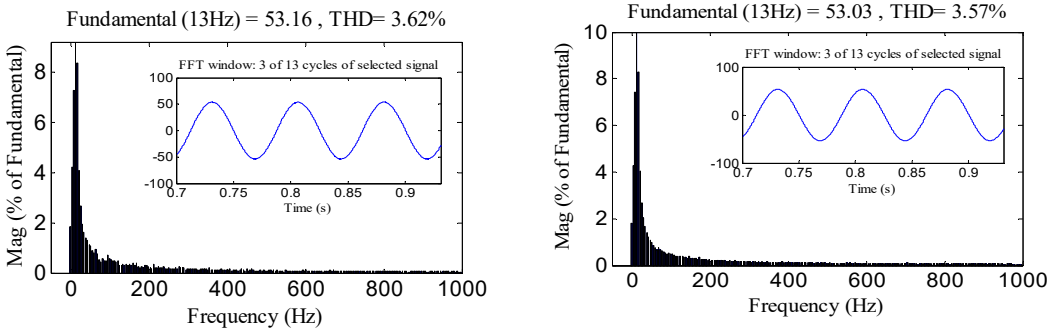

(**a**) Conventional PPC method (**b**) Proposed R-PPC method

Figure 9. Stator current frequency spectra of the unit motor under the charge state. (**a**) Conventional PPC method; (**b**) Proposed R-PPC method.

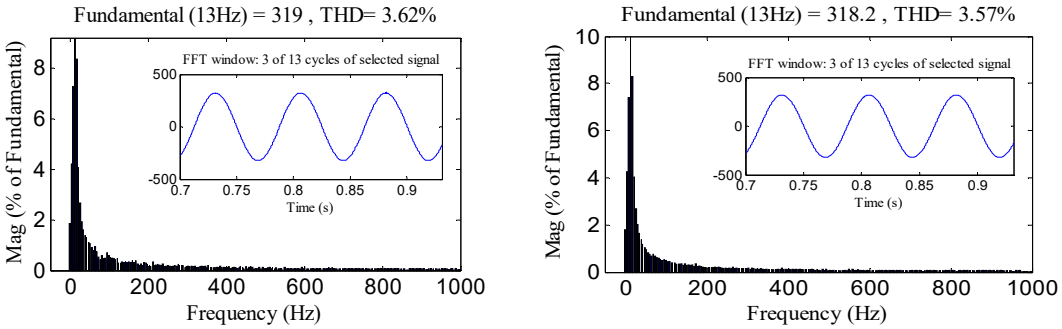

(**a**) Conventional PPC method (**b**) Proposed R-PPC method

Figure 10. Stator current frequency spectra of the 6*3-phase PMSM under the charge state. (**a**) Conventional PPC method; (**b**) Proposed R-PPC method.

The comparative simulation results of the d- and q-axis current under the inductance parameter mismatch are shown in Figure 7. The d- and q-axis current response values can accurately track the reference values, which are clearly shown in Figure 7. However, the d- and q-axis current response peak-to-peak ripple of the conventional PPC method is significantly higher than that of the proposed R-PPC strategy. From Figure 7a,b, it can be observed that the d- and q-axis current response peak-to-peak ripples of the conventional PPC method respectively reached ±8 A and ±7 A, decreasing to ±5 A and ±5 A with the use of the proposed R-PPC method. Figure 8a presents the simulation results of the conventional PPC method, and Figure 8b presents the simulation results of the proposed R-PPC method. From Figure 8a,b, it can be observed that the phase current waveform of the 6*3-phase PMSM can both keep a perfect sinusoidal waveform by adopting the conventional PPC method and the proposed R-PPC method. From Figure 9a,b, it can be seen that the stator current fundamental values of the conventional PPC method and proposed R-PPC method are respectively 53.16 A and 53.03 A, and the THDs of the conventional PPC method and proposed R-PPC method are respectively 3.62% and 3.57%. Figure 10 shows the stator current frequency spectra of the 6*3-phase PMSM under inductance parameter mismatch. It can be seen from Figure 10a that the stator current fundamental value and the THD of the conventional PPC method are 319 A and 3.62%, respectively. The stator current fundamental value and the THD of the 6*3-phase PMSM are respectively 318.2 A and 3.57% through use of the proposed R-PPC method, which can be observed in Figure 10b. According to Figures 8–10, it can be known that the inductance parameter mismatch does not affect the stator current of the 6*3-phase PMSM under the charge state. The stator current control performance of the conventional PPC method has the same superior performance as the proposed R-PPC method.

5.2. B. Control Performance Comparison between the Conventional PPC and Proposed R-PPC under the Discharge State

In order to verify the R-PPC performance of the 6*3-phase PMSM in the case of discharge state, the power reference of discharge state is given as:

$$\begin{cases} P^{ref} = -1.6 \times 10^5 t - 0.8 \times 10^5 & 0 \le t \le 0.5s \\ P^{ref} = -1.6 \times 10^5 & 0.5s \le t \le 1s \end{cases} \quad (27)$$

In this simulation, in order to simulate the inductance parameter mismatch, the inductance parameter value is also set as 50% of the initial value. The comparative simulation results of the conventional PPC method and the proposed R-PPC method under the discharge state are given in Figures 11–15. Figure 11 shows the comparative simulation results of the phase current and torque under the inductance parameter mismatch. From Figure 11, it can be seen that the torque ripple of the conventional PPC method and the proposed R-PPC method are ±280 N·m and ±160 N·m, respectively. It can be known that the peak-

to-peak torque ripple of the 6*3-phase PMSM with inductance parameter mismatch can be obviously suppressed by using the proposed R-PPC method. The comparative simulation results of the d- and q-axis current under the discharge state are shown in Figure 12. From Figure 12, it can be known that the d- and q-axis current response values can accurately track the reference values under inductance parameter mismatch. It can be observed from Figure 12a that the d- and q-axis current response peak-to-peak ripples of the conventional PPC method are ±8 A and ±7 A, respectively. The peak-to-peak ripples of the d- and q-axis current response decrease to ±4 A and ±5 A through the use of the proposed R-PPC method, as clearly shown in Figure 12b. Figure 13 shows the comparative simulation results of the phase current under the inductance parameter mismatch. It can be observed from Figure 13 that the 6*3-phase PMSM with inductance parameter mismatch can achieve a perfect sinusoidal waveform using both the conventional PPC method and the proposed R-PPC method.

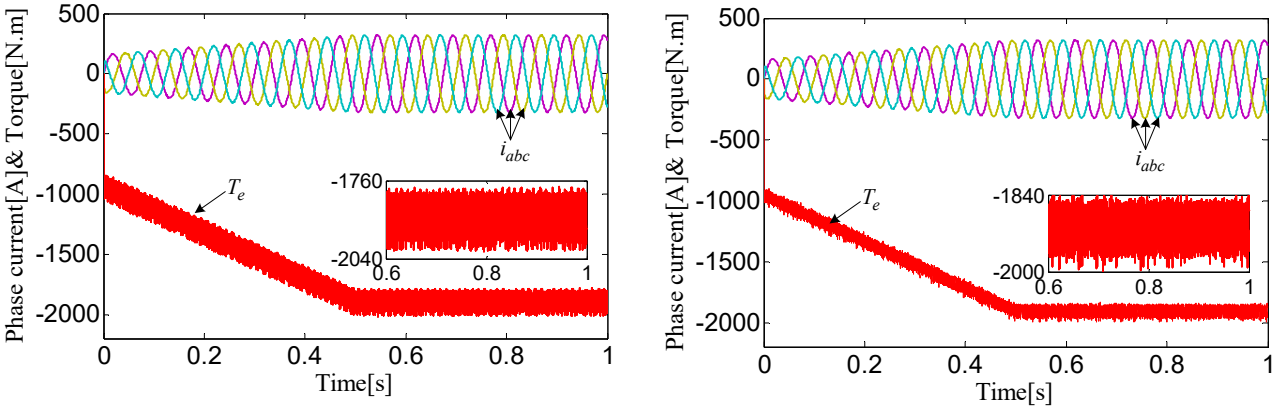

Figure 11. Simulation results of the phase current and torque under the discharge state. (**a**) Conventional PPC method; (**b**) Proposed R-PPC method.

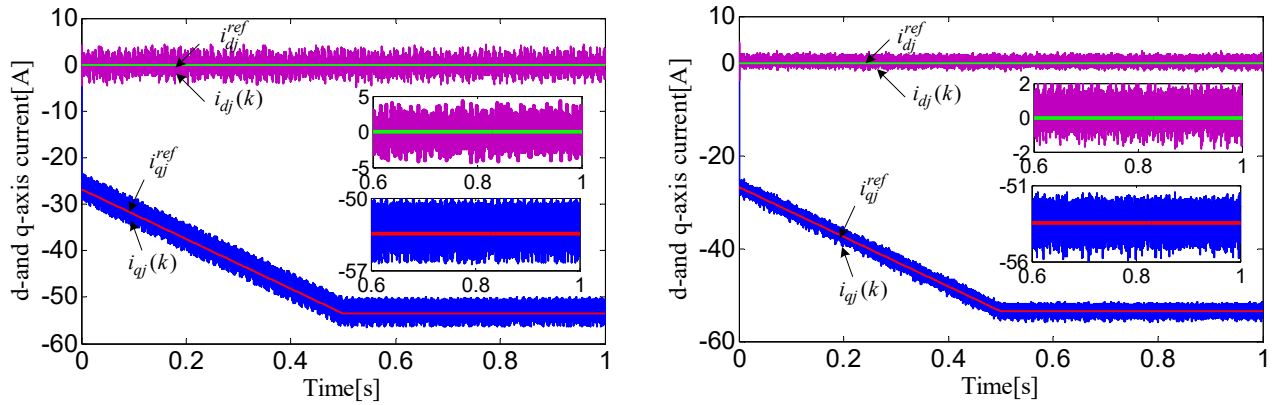

Figure 12. Simulation results of the d- and q-axis current under the discharge state. (**a**) Conventional PPC method; (**b**) Proposed R-PPC method.

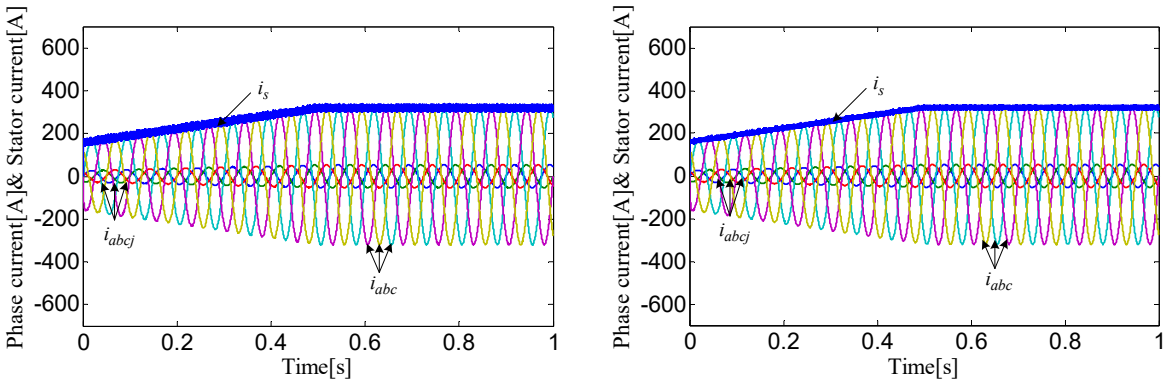

(**a**) Conventional PPC method (**b**) Proposed R-PPC method

Figure 13. Simulation results of the phase current under the discharge state. (**a**) Conventional PPC method; (**b**) Proposed R-PPC method.

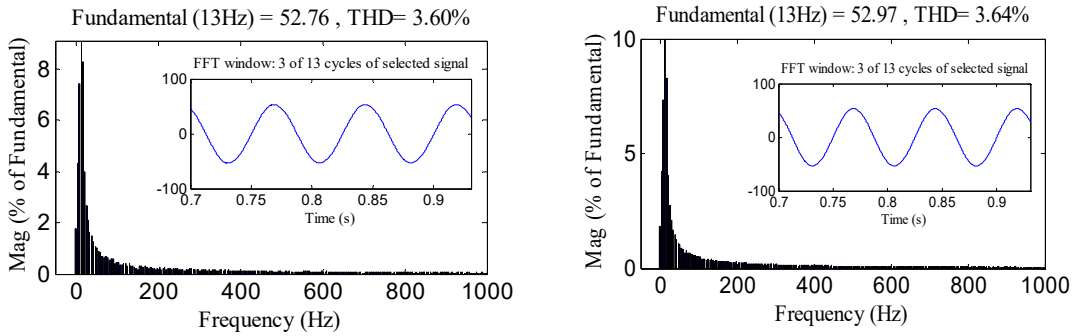

(**a**) Conventional PPC method (**b**) Proposed R-PPC method

Figure 14. Stator current frequency spectra of the unit motor under the discharge state. (**a**) Conventional PPC method; (**b**) Proposed R-PPC method.

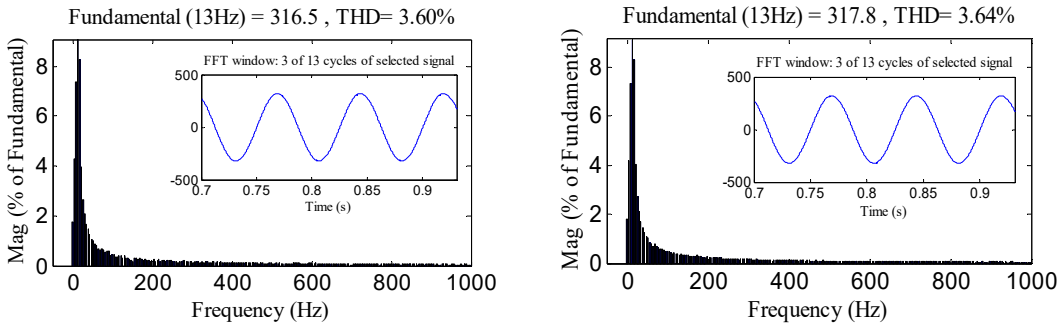

(**a**) Conventional PPC method (**b**) Proposed R-PPC method

Figure 15. Stator current frequency spectra of the 6*3-phase PMSM under the discharge state. (**a**) Conventional PPC method; (**b**) Proposed R-PPC method.

It can be seen from Figure 14a that the stator current fundamental values and THD of the unit motor are respectively 52.76 A and 3.6% when the conventional PPC method is adopted. It can be seen from Figure 14b that the stator current fundamental values and THD of the proposed R-PPC method are 52.97 A and 3.64%, respectively. The stator current frequency spectra of the 6*3-phase PMSM with inductance parameter mismatch is illustrated in Figure 15. From Figure 15a, it can be known that the stator current fundamental value and the THD of the 6*3-phase PMSM with the conventional PPC

method are 316.5 A and 3.6%, respectively. The stator current fundamental value and the THD of the 6*3-phase PMSM with the proposed R-PPC method are respectively 317.8 A and 3.64%, as clearly observed in Figure 15b. From Figures 14 and 15, it can be known that stator current THD of the 6*3-phase PMSM and unit motor is the same when the conventional PPC and proposed R-PPC methods are used. According to the simulation analysis, it can be known that inductance parameters mismatch does not affect the stator current of the 6*3-phase PMSM.

6. Experimental Results

Taking the 6*3-phase PMSM as an example, the RT-Lab hardware-in-the-loop simulation (HILS) platform is established to verify the feasibility and effectiveness of the proposed R-PPC method under the inductance parameter mismatch. The RT-Lab HILS platform consists of a DSP controller, OP5600 simulation motor, and other computer monitoring interfaces. The parameters of the RT-Lab HILS platform are consistent with those of the simulation. Comparative experimental results of the conventional PPC method and the proposed R-PPC method under the charge state and discharge state are given in Figures 16–19.

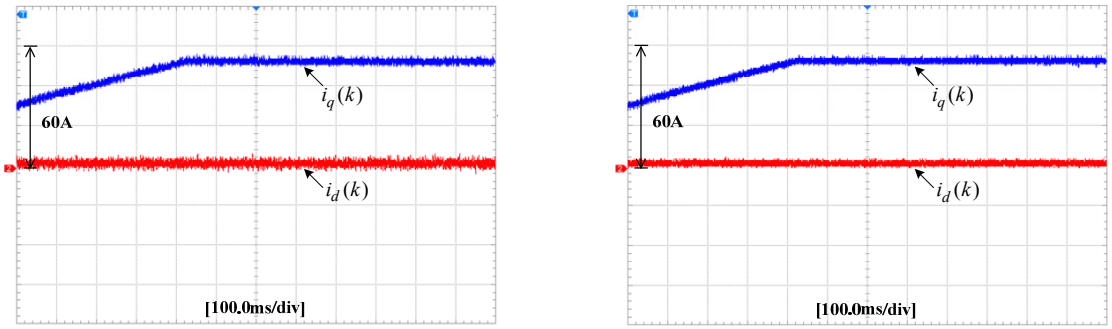

(**a**) Conventional PPC method (**b**) Proposed R-PPC method

Figure 16. Experimental results of the d- and q-axis current under the charge state. (**a**) Conventional PPC method; (**b**) Proposed R-PPC method.

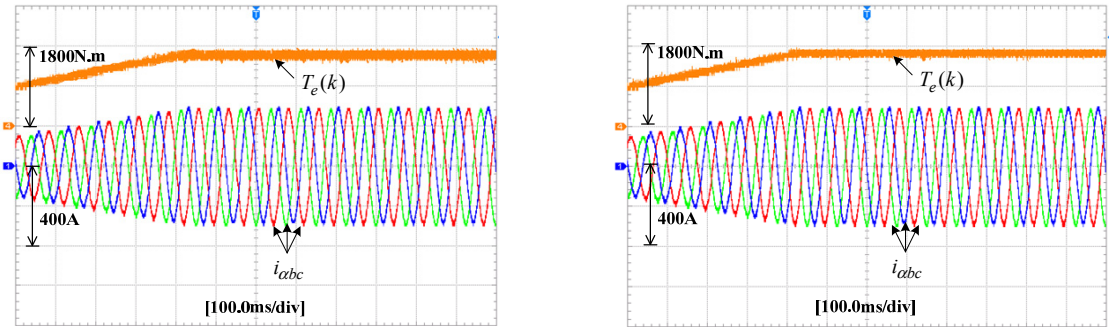

(**a**) Conventional PPC method (**b**) Proposed R-PPC method

Figure 17. Experimental results of the phase current and torque under the charge state. (**a**) Conventional PPC method; (**b**) Proposed R-PPC method.

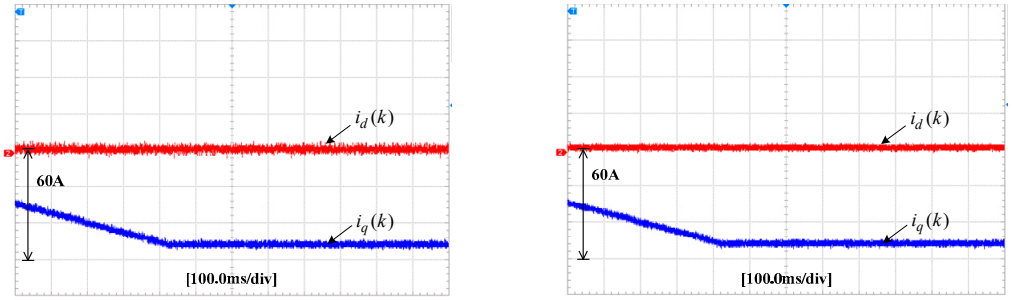

(**a**) Conventional PPC method (**b**) Proposed R-PPC method

Figure 18. Experimental results of the d- and q-axis current under the discharge state. (**a**) Conventional PPC method; (**b**) Proposed R-PPC method.

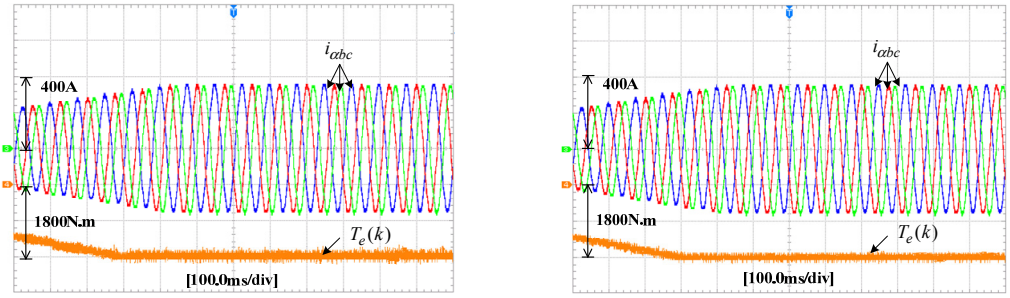

(**a**) Conventional PPC method (**b**) Proposed R-PPC method

Figure 19. Experimental results of the phase current and torque under the discharge state. (**a**) Conventional PPC method; (**b**) Proposed R-PPC method.

Figure 16 presents the comparative experimental results of the d- and q-axis current under the charge state. From Figure 16a, it can be seen that the d- and q-axis current response ripple of the conventional PPC method is obviously higher than that of the proposed R-PPC method in the case of inductance parameter mismatch. When the proposed R-PPC method is applied, the ripple of the d-axis current response value is obviously suppressed under the inductance parameter mismatch, as shown in Figure 16b. Figure 17 illustrates the comparative experimental results of the phase current and torque under the charge state. From Figure 17a, it is known that the peak-to-peak torque ripple of steady-state operation is significantly high by using the conventional PPC method. It can be observed from Figure 17b that the peak-to-peak torque ripple of proposed R-PPC method is obviously lower than that of the conventional PPC method in the case of inductance parameter mismatch. Therefore, it can be seen from Figures 17 and 18 that the current response ripple and torque ripple of *N**3-phase PMSM with the inductance parameter mismatch are obviously suppressed through the adoption of the proposed R-PPC method.

Figure 18 shows the d- and q-axis response current experimental results of the conventional PPC method and the proposed R-PPC method under the discharge state. It can be seen from Figure 18 that the q-axis response current ripple of the conventional PPC method is consistent with that of the proposed R-PPC method in the case of inductance parameter mismatch. However, the d-axis current response ripple of the proposed R-PPC method is significantly lower than that of the conventional PPC method under the inductance parameter mismatch, as clearly shown in Figure 18b. The phase current and torque experimental results of the conventional PPC method and the proposed R-PPC method under the inductance parameter mismatch are shown in Figure 19. From Figure 19a, it can be known that the inductance parameter mismatch will lead to the increase torque ripple of the 6*3-phase PMSM under the discharge state. The peak-to-peak torque ripple of the 6*3-phase PMSM is obviously suppressed when the proposed R-PPC method is adopted in

the case of inductance parameter mismatch, which can clearly be observed in Figure 19b. From Figures 18 and 19, it can be known that the control performance of the proposed R-PPC method for the 6*3-phase PMSM is obviously better than that of the traditional control method in the case of inductance parameter mismatch.

7. Conclusions

This paper present the R-PPC method to track its reference power for an *N**3-phase PMSM with inductance parameter mismatch, which can improve robustness against inductance parameter mismatch and eliminate the one-beat delay in the digital control system. In addition, a novel R-PPC technique using robustness factors is employed for the design to strengthen the robustness against inductance parameters for the *N**3-phase PMSMs. The appropriate robustness factors were selected so as to achieve the excellent power control performance under both charge and discharge states. Therefore, the *N**3-phase PMSM operates well in the case of the discharge state and charge state, meanwhile obtaining a good steady-state control performance. Compared with the conventional PPC method, the results verity that the proposed R-PPC can obtain the merits of less torque ripple and lower d- and q-axis response current ripples under inductance parameter mismatch.

Author Contributions: W.Z. and Y.L. designed the proposed control strategy, G.W. and Z.R. conducted experimental works, J.G. and D.L. gave help of paper writing. All authors have read and agreed to the published version of the manuscript.

Funding: This work was supported in part by the National Natural Science Foundation of China (51577052).

Conflicts of Interest: The authors declare no conflict of interest.

References

1. Demir, Y.; Aydin, M. A novel dual three-phase permanent magnet synchronous motor with asymmetric stator winding. *IEEE Trans. Magn.* **2016**, *52*, 1–5. [CrossRef]
2. Rao, Z.; Zhang, Z.; Huang, S.; Long, Z.; Wu, G. Characteristics and current harmonic control of N* three-phase PMSG for HVDC transmission Based on MMC. *Energies* **2020**, *13*, 178. [CrossRef]
3. Dwari, S.; Parsa, L. An optimal control technique for multiphase PM machines under open-circuit faults. *IEEE Trans. Ind. Electron.* **2008**, *55*, 1988–1995. [CrossRef]
4. Zhang, W.; Wu, G.; Rao, Z.; Zheng, J.; Luo, D. Predictive Power Control of Novel N*3-phase PM Energy Storage Motor for Urban Rail Transit. *Energies* **2020**, *15*, 1578. [CrossRef]
5. Han, X.; Jiang, D.; Zou, T.; Qu, R. Two-segment three-phase PMSM drive with carrier phase-shift PWM for torque ripple and vibration reduction. *IEEE Trans. Power Electron.* **2019**, *34*, 588–599. [CrossRef]
6. Morel, F.; Shi, X.; Retif, J. A comparative study of predictive current control schemes for a permanent-magnet synchronous machine drive. *IEEE Trans. Ind. Electron.* **2009**, *56*, 2715–2728. [CrossRef]
7. Li, S.; Liu, Z. Adaptive speed control for permanent magnet synchronous motor system with variations of load inertia. *IEEE Trans. Ind. Electron.* **2009**, *56*, 3050–3059.
8. Tong, L. An SRF-PLL-based sensorless vector control using the predictive deadbeat algorithm for the direct-driven permanent magnet synchronous generator. *IEEE Trans. Power Electron.* **2014**, *29*, 2837–2849. [CrossRef]
9. Wu, G.; Huang, S.; Wu, Q.; Rong, F.; Zhang, C.; Liao, W. Robust Predictive Torque Control of N∗3-Phase PMSM for High-Power Traction Application. *IEEE Trans. Power Electron.* **2020**, *35*, 10799–10809. [CrossRef]
10. Wu, G.; Huang, S.; Wu, Q.; Zhang, C.; Rong, F.; Hu, Y. Predictive Torque and Stator Flux Control for N∗3-Phase PMSM Drives with Parameter Robustness Improvement. *IEEE Trans. Power Electron.* **2021**, *36*, 1970–1983. [CrossRef]
11. Cortes, P.; Rodriguez, J.; Silva, C. Delay compensation in model predictive current control of a three-phase inverter. *IEEE Trans. Ind. Electron.* **2012**, *59*, 1323–1325. [CrossRef]
12. Zhang, C.; Wu, G.; Rong, F.; Feng, J.; Jia, L.; He, J.; Huang, S. Robust fault-tolerant predictive current control for permanent magnet synchronous motors considering demagnetization fault. *IEEE Trans. Ind. Electron.* **2017**, *65*, 5324–5334. [CrossRef]
13. Zhang, X.; Hou, B.; Mei, Y. Deadbeat predictive current control of permanent-magnet synchronous motors with stator current and disturbance observer. *IEEE Trans. Power Electron.* **2016**, *32*, 3818–3834. [CrossRef]
14. Sozer, Y.; Torrey, D.A.; Mese, E. Adaptive predictive current control technique for permanent magnet synchronous motors. *IET Power Electron.* **2013**, *6*, 9–19. [CrossRef]
15. Huang, S.; Wu, G.; Rong, F.; Zhang, C.; Huang, S.; Wu, Q. Novel predictive stator flux control techniques for PMSM drives. *IEEE Trans. Power Electron.* **2018**, *34*, 8916–8929. [CrossRef]

16. Lyu, M.; Wu, G.; Luo, D.; Rong, F.; Huang, S. Robust nonlinear predictive current control techniques for PMSM. *Energies* **2019**, *12*, 443. [CrossRef]
17. Moreno, J.C.; Huerta, J.M.; Gil, R.G.; Gonzalez, S.A. A robust predictive current control for three-phase grid-connected inverters. *IEEE Trans. Ind. Electron.* **2009**, *56*, 1993–2004. [CrossRef]
18. Yang, M.; Lang, X.; Long, J.; Xu, D. Flux immunity robust predictive current control with incremental model and extended state observer for PMSM drive. *IEEE Trans. Power Electron.* **2017**, *32*, 9267–9279. [CrossRef]
19. Yang, J.; Zheng, W.X.; Li, S.; Wu, B.; Cheng, M. Design of a prediction-accuracy-enhanced continuous-time MPC for disturbed systems via a disturbance observer. *IEEE Trans. Ind. Electron.* **2015**, *62*, 5807–5816. [CrossRef]
20. Yang, J.; Li, S.; Yu, X. Sliding-mode control for systems with mismatched uncertainties via a disturbance observer. *IEEE Trans. Ind. Electron.* **2012**, *60*, 160–169. [CrossRef]
21. Young, H.A.; Perez, M.A.; Rodriguez, J. Analysis of finite-control-set model predictive current control with model parameter mismatch in a three-phase inverter. *IEEE Trans. Ind. Electron.* **2016**, *63*, 3100–3107. [CrossRef]
22. Xia, C.; Wang, M.; Song, Z.; Liu, T. Robust model predictive current control of three-phase voltage source PWM rectifier with online disturbance observation. *IEEE Trans. Ind. Electron.* **2012**, *8*, 459–471. [CrossRef]
23. Rubagotti, M.; Raimondo, D.M.; Ferrara, A.; Magni, L. Robust model predictive control with integral sliding mode in continuous-time sampled-data nonlinear systems. *IEEE Trans. Autom. Control* **2010**, *56*, 556–570. [CrossRef]
24. Liu, H.; Li, S. Speed control for PMSM servo system using predictive functional control and extended state observer. *IEEE Trans. Ind. Electron.* **2011**, *59*, 1171–1183. [CrossRef]
25. Hu, F.; Luo, D.; Luo, C.; Long, Z.; Wu, G. Cascaded robust fault-tolerant predictive control for PMSM drives. *Energies* **2018**, *11*, 3087. [CrossRef]